Supporting Online Material for

Synchrony of Thalamocortical Inputs Maximizes Cortical Reliability

Hsi-Ping Wang,* Donald Spencer, Jean-Marc Fellous, Terrence J. Sejnowski

*To whom correspondence should be addressed. E-mail: ping@salk.edu

Published 2 April 2010, *Science* **328**, 106 (2010)
DOI: 10.1126/science.1183108

This PDF file includes:

Supporting Online Material for

Synchrony of Thalamocortical Inputs Maximizes Cortical Reliability

Hsi-Ping Wang[+], Donald Spencer, Jean-Marc Fellous, and Terrence J. Sejnowski

[+]To whom correspondence should be addressed:

E-mail: ping@salk.edu (H.-P. W.); dspencer@salk.edu (D. S.);

fellous@email.arizona.edu (J.-M. F.); terry@salk.edu (T. J. S.).

This PDF file includes:

METHODS

General

The goal of this paper is to better understand the role of synchrony in information transfer in the primary visual thalamocortical pathway through analysis of the best existing experimental data. The model allowed us to draw conclusions from the experimental data reported in Kara et al *(S1)* and reach conclusions that were not otherwise possible. We began by developing data analysis tools specific to the Kara et al. experimental paradigm of many (200 or more) repeated trials with an identical drifting grating pattern stimulus of 250 msec duration. We confirmed proper data extraction and analysis of the Kara data by comparing our calculations of rastergrams, Fano Factor (vs. counting window) and PSTH with the values reported in their paper (S*1*). In all cases, for the triple recordings from retina, LGN and cortex, there was a perfect match. This gave confidence that our calculations of reliability, which is weakly related to Fano Factor and was not calculated in (S*1*), would also be valid.

We next created a multi-compartment model of a reconstructed spiny stellate neuron from the cat V1 with separate synaptic inputs (both inhibitory and excitatory) from LGN and the cortex. Using LGN input patterns recorded during drifting grating presentations in the anesthetized cat (S*1*) as inputs, we investigated the effects on the reliability of the cell of the number and synchrony of LGN afferent synapses in the presence of feedforward inhibition and background cortical activity. The input "driver" spike trains from LGN included the effects of jitter, noise spikes, and bursting. We finally compared these outputs to the actual recorded data from the various experimental studies upon which the inputs were based (S*1-3*).

Spiny stellate cell model

All simulations were conducted on a Hodgkin-Huxley multi-compartment neuron model using the NEURON version 6.0 simulation environment (S*4*). We used a digitally reconstructed spiny stellate cell of the cat V1 region, layer 4 (S*5-7*), consisting of 744 compartments (Fig. 1a), subdivided into 6 dendritic branches. All dendritic branches were divided into cylindrical compartments with a maximum length of 50 μm. The dendritic

membrane area of spiny neurons was increased to account for spines (adding 0.83 μm^2 per linear μm of dendrite).

The soma area was 779 μm^2, the total dendritic area was 22,491 μm^2 and the perisomatic area (where GABAergic synapses were located, see below) was 2032 μm^2. We added an axonal segment of length 250 μm and total area of 95 μm^2 for spike generation.

The input resistance was measured to be from 10-15MΩ, which is consistent with in vivo recordings of cells in an up state in an anaesthetized cat (S*8*).

Feedforward inhibitory neuron model

Furthermore, we simulated a feedforward inhibitory neuron which receives input from LGN and synapses onto the stellate cell. The cell was adapted from one used by Bush et al (S*9*) and is available for download from ModelDB (S*10*). The cell consists of 5 compartments, which include a soma and 4 dendritic branches. Each compartment contains an AMPA excitatory synapse driven by the same LGN input as the V1 neuron. If the cell spikes, this is transmitted to the SSC cell via a GABA synapse with the same conductance strength as a normal intracortical GABAergic synapse (*Gmax* = 0.05 nS) multiplied by a synaptic number multiplier representing the number of synaptic connections that this feedforward connection makes. The default used in all experiments is 200 synapses connection strength, except for Fig. 4B, in which a variety of strengths are used to determine the effects of inhibitory feedforward connection strength on SSC response.

Currents

All currents were temperature dependent ($Q_{10} = 3$), and the temperature was set at 36°C. The global axial resistance was set at 100 Ωcm and the membrane capacitance was set to 1.7 $\mu F/cm^2$ to account for the presence of spines (S*11*). All currents were calculated using conventional Hodgkin-Huxley-style kinetics with an integration time step of 100 μs. Currents *(I)* for most channels are given by:

$$I = ga^x b(V - E) \qquad (1)$$

where *g* is the local conductance density, *a* is an activation variable with *x* order kinetics, *b* is an optional inactivation variable, V is the local membrane potential, and E is the reversal potential for the ionic species.

The somatic compartment contained delayed rectifier potassium (reversal potential, $E_K = -80$ mV) and fast sodium (reversal potential, $E_{Na} = 50$ mV) currents responsible for spike generation (S*12*). As in (S*5*) the soma also contained a high voltage activated (HVA) calcium current, I_{Ca} (S*13*), with a calcium pump (S*14*). Internal calcium concentration was computed using entry via I_{Ca} and removal by a first order pump:

$$\frac{d[Ca_{2+}]_i}{dt} = (-10^5 * I_{ca} / 2F) - ([Ca_{2+}]_i - [Ca_{2+}]_\infty)/\tau_R \qquad (2)$$

where $[Ca2+]_\infty = 0.1$ μM, and $\tau_R = 100$msec, and F is the faraday constant.
A slow non-inactivating potassium current was added to allow for spike frequency adaptation (S*15*). Except for the specified reversal potentials, and specified different calcium concentration and decay rates (shown above), the above currents used the same parameters, including channel activation and inactivation variables as specified in the downloadable model (S*5*).

In addition to the above channels, a slow after hyper polarization (AHP) calcium-activated potassium current was added to control bursting (S*16*) ($\tau_R = 0.1$, $E_K = -80$ mV, $g_{kbar} = 0.018$ nS). We also added a slow, non-inactivating somatic M current to allow for spike frequency adaptation (S*15*-*S17*). The following equations are solved at each time step:

$$n_\infty = 1/(1+e^{(-(V+35)/10)}) \qquad (3)$$

$$\tau_n = 1000 /(3.3*(e^{((V+35)/40)}+e^{(-(V+35)/20))}) \qquad (4)$$

$$n' = (n_\infty - n) / \tau_n \qquad (5)$$

where n_∞ is the state variable at steady state , V is the membrane potential, and τ_n is the time constant. (g_{bar} = 0.01 S/cm2).

The axonal section has fast sodium currents and delayed rectifier currents based on Traub et al (S*12*). (V = -64mV, g_{Nabar} = 0.1 nS, g_{Kbar} = 0.05 nS)

Parameter values for the neuron model and all currents are shown in Table 1.

Because the precise distribution of dendritic ion channels is still largely unknown for these cells (S*18*-*S19*), we focused our study on a passive dendritic tree. The distribution of leak channels reflected, however, the fact that dendrites were more 'leaky' than the soma (S*11*) and as a consequence we distributed these channels in a graded manner according to:

$$R_m(d) = R_{end} + \frac{R_{soma} - R_{end}}{1 + e^{(d_{half} - d)/s}} \qquad (6)$$

where d_{half} is the distance at which the function is halfway between R_{soma} and R_{end}, and s determines the steepness of the decay from R_{soma} to R_{end} with distance d from the soma to all dendritic compartments (S*11*). We used s = 50 μm, R_{soma} = 33,333 Ωcm^2 and R_{end} = 10,000 Ωcm^2. As a control, for some simulations we also added active dendritic currents based on the same spiny stellate cell model(S*5*) (results published separately).

For the inhibitory interneuron cell, the parameters for the various currents are unchanged from the original ModelDB download (S*10*) and are listed in Table 2.

Active dendrites

For some simulations, dendrites were made active as in previous work (S*5*). Specifically, three voltage dependent currents and one Ca^{2+}- dependent current were added to the passive dendrites using the same Hodgkin – Huxley kinetic formalism (reversal potentials, activation variables, reaction rate functions). These included fast Na^+ channels, slow non-inactivating K^+ channels (responsible for after-hyperpolarization), and high-threshold Ca^{2+} channels, which were uniformly distributed throughout the dendritic arbor. Although there are a wide variety of dendritic currents in neocortical

dendrites, this model has been shown to be sufficient to reproduce a number of firing features seen in cortical cells (S*5*).

Synapses

Of the approximately 5,000-10,000 synapses on layer 4 (L4) spiny stellate cells, only about 6% to 15% are excitatory thalamic afferents (S*20*). The other inputs consist of approximately 80% excitatory and 20% inhibitory synapses (S*6*). In our model, we simulated 300 LGN excitatory synapses, 4,500 intracortical (from L4 and L6) excitatory glutamatergic synapses, and 1,000 inhibitory GABAergic synapses. All excitatory synapses were randomly distributed (i.e., separation distances drawn from auniform distribution) throughout the dendritic tree and soma, while the inhibitory inputs resided perisomatically on dendrites within 200 microns of the soma (uniformly distributed). For the experiments, we introduced structured spike train patterns presynaptically into the 300 LGN synapses to simulate behavioral spike trains seen in vivo (S*3*). The 5,500 other synapses were considered to contribute only background noise through excitatory and inhibitory currents and they were stimulated by independent random spike trains with Poisson distributed arrival times.

All synapses were implemented explicitly as point processes with a continuously integrated kinetic scheme that described an alpha function, allowing for summation (S*21*). For each simulation, the 300 LGN AMPA synapses (time constant 3 msec, reversal potential 0 mV, G_{max} = 0.65 nS, (S*23*)), were activated by a mixture of Poisson presynaptic spike times (noise), and precise spike times forming presynaptic patterns (signals). The precise rates and timing of these spike times varied for each simulation. The background presynaptic firing rate of the intracortical excitatory synapses (time constant 3 msec, reversal potential 0 mV) was set to Poisson trains with rate 1 spike/sec while the inhibitory GABA synapses (time constant 5 msec, reversal potential -70 mV) released faster at about 5 spikes/sec Poisson based on estimates obtained from awake animals in vivo (S*22*). The conductances of the background excitatory (G_{max} = 0.64 nS) and inhibitory synapses (G_{max} = 0.05 nS) were based on in vivo estimates then adjusted to simultaneously achieve a firing rate of about 3 spikes/sec and a membrane potential fluctuation of 3 mV in the absence of any LGN stimulation, based on values selected in

accordance to in vivo conditions of a cortical cell stimulated by background activity alone (S*24*)

Dynamic stochastic synapses

One important property of excitatory synapses is that they exhibit short-term facilitation and depression which increase and decrease, respectively, the probability of neurotransmitter release according to the history of preceding spikes over the last several hundred milliseconds (S*25*). In computational models, these dynamics are traditionally incorporated phenomenologically (S*26-S27*) so as to vary the level of facilitation and depression based on the measured average responses of a large group of synapses. However, these models do not capture the stochasticity of individual synapses that only initially release vesicles on the order of 20% of the time on average (S*28*). This stochasticity of individual synapses is an important source of unreliability, which we included in the model.

The dynamic stochastic synapse we used was based on previous experiments and theoretical formulation using minimal stimulation (S*29-S30*). The probability of release is characterized by the equation

$$P_r(t) = 1 - e^{-F(t)D(t)} \tag{7}$$

where F(t) and D(t) represent facilitation and depression levels, respectively, and

$$F(t) = F_0 + \sum_{t_i<t} f(t-t_i) \text{ and } f(s) = \alpha e^{-s/\tau} \tag{8}$$

describes an exponentially decaying accumulation of calcium with each presynaptic spike at time t_i (F_0, α and τ are constants), and

$$D(t) = \max(0, D_0 - \sum_{t_i<t, t_i \in S} d(t-t_i)) \text{ and } d(s) = \beta e^{-s/\tau'} \tag{9}$$

where S is the dynamically updated set of spike times that yielded release (D_0, β, τ' are constants). For all simulations, we used F_0= 0.003, D_0= 60 (yielding an initial probability

of release of 0.2), the magnitude of depression was set to α= 0.02, and the magnitude of facilitation was set to β = 50. The time constants were set to τ = 94 msec and τ' = 380 msec. With these values, the response to regular trains of action potentials injected simultaneously to 100 synapses distributed randomly consisted of EPSP sequences that mimicked in amplitude and dynamics those obtained in vitro and in phenomenological models (S*26*).

At each excitatory synapse, when a presynaptic spike is received at time t, the probability of release, $P_r(t)$, is calculated based on the current spike history S. A random number from a uniform distribution is then drawn and if the random number is larger than $P_r(t)$, a postsynaptic potential is generated, and S is updated. Note that it is not necessary to update $P_r(t)$ for each synapse at every simulation time increment – only when a presynaptic spike occurs at that synapse.

The dynamic synapse model was used for all excitatory synapses, both from LGN and from intracortical presynaptic neurons. For inhibitory synapses, release was reliable and occurred with the arrival of each spike in the pre-synaptic train. Although there is some evidence that thalamocortical synapses have a high and largely invariant probability of release (S*31-S32*), other studies indicate the possibility of weak synapses (S*33*). Thus, for the purpose of this experiment, we took into account the worst case scenario by treating intracortical and thalamocortical synapses as equally weak and probabilistic. However, some experiments were conducted in which probabilistic neurotransmitter release was removed from the LGN synapses.

Simulation Paradigm

The time step in the NEURON simulations was set at dt = 0.1 msec and the total duration of a trial varied from 250 milliseconds to 10 seconds. The first 50 msec of each simulation were considered to be numerical transients, and were discarded from all analyses. For a set of trials the LGN inputs consisted of a pattern of 'event' spikes which were received simultaneously (but with some random jitter from synapse to synapse) by some designated subset of the synapses. These event spike trains were from actual recordings of LGN neurons made by Kara et al *(S1)* in anesthetized cats stimulated by drifting gratings. The number of LGN synapses receiving these event spike trains was

designated the synchrony magnitude. For example, a synchrony magnitude of 100 synapses means that 100 synapses receive a particular set of events simultaneously. Additional Poisson distributed noise spikes were added to all of the LGN synapses. To determine reliability, different sets of presynaptic spike trains from the LGN recordings were then input to the LGN synapses for each trial, (unlike the "frozen noise" approach (S*34*), which utilizes identical inputs across trials). Thus, although the presynaptic spike trains were similar, they were not identical across trials - the added input variability corresponded to additional variability to be expected at the transformation from the retina to the LGN, dynamic stochastic synapses and random background noise fluctuations.

Recordings from 4 cells were used, each having at least 100-200 trials/cycles. All of these data were used in Figure 3 in producing firing rate and reliability comparisons. Only 30 distinct trials were used for each data point in Fig 2.

Calculation of Fano Factor

Our calculations of Fano Factor used the same technique of overlapping time counting windows described under Methods in (S*1*). Fano Factor is defined as:

$$F = \frac{\sigma^2{}_W}{\mu_W} \tag{10}$$

where $\sigma^2{}_W$ is the variance and μ_W is the mean of the firing rate (total spike count) in time window *W*. In most simulations, W = 250 msec. This was selected after performing a series of tuning experiments to determine the affect of the size of W to find the minimal Fano factor (Fig. S2). Counting windows were varied, within a trial, from 1 msec to 250 msec (the length of the trial). This analysis reveals the effects of spike count variability over different periods in the trial, averaged over all trials. Traditionally, the counting window with minimum Fano Factor is quoted as the correct value. Fig. S2 compares Fano Factor counting window analysis of the original Kara data for a V1 cortical cell with that of our spiny stellate model cell driven by the Kara et al spike trains recorded in the LGN (S*1*). It can be seen that the minimum Fano Factor occurs in the range of 50 msec in both cases. This implies that there is a strong statistical similarity between our model stellate cell, which integrates all that is commonly known about cell physiology in

the thalamocortical pathway, and the recorded cortical cells in cat when presented with identical spike trains.

Using the same output data from the spiny stellate cell that was used for Fig. 2, the Fano Factor was computed for each synchrony magnitude using a 50 msec counting window. The result, plotted in Fig. S2C, shows a distinct drop in spike count variability by synchrony magnitude 20 synapses indicating a measurable information transfer. The Fano Factor remains low through 80 synapses and rises thereafter, possibly due to shunting inhibition and/or to synaptic depression. This plot also indicates an inverse correlation between Fano Factor and our reliability measure as seen by comparing Fig. S2C and Fig. 2A.

Calculation of reliability

Reliability was computed using a synchrony-based measure (S*35*) applied to the spike train output of the model neuron. Briefly, the spike trains obtained from *N* repeated presentations of the same stimulus were each convolved with a Gaussian filter of width 2σ (σ is the width of the Gaussian kernel in msec) with $\vec{s}_i$ denoting the *i*th smoothed train. After convolving all *N* trials, the inner product is taken between all pairs of trials (each trial normalized by its norm), the inner products are summed, and the sum is divided by the number of pairs to yield a reliability measure on the interval (0,1). Formally, the reliability *R* is defined as

$$R = \frac{2}{N(N-1)} \sum_{i=1}^{N} \sum_{j=i+1}^{N} \frac{\vec{s}_i \cdot \vec{s}_j}{\left|\vec{s}_i\right| \cdot \left|\vec{s}_j\right|} \tag{11}$$

We used $\sigma = 3$ msec, $N = 30$ trials based on the observation that reliable events in the experimental data for V1 cells occur with a jitter of approximately 3 msec (S*36*). The choice of 30 trials was found to provide consistently good estimates of *R* without running excessively many trials (data not shown).

This reliability metric had a bias for higher firing rates because an increase in overall spike density inevitably caused more overlap with input spikes and thus increased the measured spike timing reliability (STR) level. This effect was quantified in a control test

measuring STR with purely random (Poisson) input spike trains on the LGN synapses at differing (0 – 20 spikes per second) arrival rates (results not shown). In Fig. 3-6, to facilitate comparison of control factors, we compensated by subtracting the reliability due to noise, which can be found when pure noise (and no signal events) are present in the synaptic input. Thus, these graphs all have STR curves which start at the origin.

In earlier studies (S*34*), the terms reliability and precision were related but separately measured quantities. The metric used in our study, which we simply refer to as reliability, actually incorporates both reliability as well as precision in the earlier senses.

Both reliability and precision of spiking are needed for a neuron to successfully decode information contained in the patterns of input spikes. Note that the output of the neuron need not reproduce the input pattern, but may respond with a different pattern of spikes. Our measure of reliability picks up these output spike patterns irrespective of the input patterns.

Calculation of Reliability Per Spike (RPS)

The reliability, R, of a set of 30 trials was computed (S*35*), and was divided by the ratio of the average firing rate, FR_{ave}, over the maximum observed firing rate, FR_{max} of the entire series of experiments (from 0 – 300 synchronous synapses).

$$RPS = \frac{R}{FR_{\text{ave}} / FR_{\max}} \tag{12}$$

Calculation of Reliability Per Synchrony Magnitude (RPSM)

The reliability, R, of a set of 30 trials was computed (S*35*), and was divided by the synchrony magnitude (SM) that was used for that set of trials.

$$RPSM = \frac{R}{SM} \tag{13}$$

Notes (Supporting online material)

S1. P. Kara, P. Reinagel, R. C. Reid, *Neuron* **27**, 635 (2000).

S2. P. Kara, R. C. Reid, *J Neurosci* **23**, 8547 (2003).

S3. P. Reinagel, R. C. Reid, *J Neurosci* **20**, 5392 (2000).

S4. M. L. Hines, N. T. Carnevale, *Neural Comput* **9**, 1179 (1997).

S5. Z. F. Mainen, T. J. Sejnowski, *Nature* **382**, 363 (1996).

S6. J. C. Anderson, R. J. Douglas, K. A. Martin, J. C. Nelson, *J Comp Neurol* **341**, 25 (1994).

S7. J. C. Anderson, R. J. Douglas, K. A. Martin, J. C. Nelson, *J Comp Neurol* **341**, 16 (1994).

S8. A. Destexhe, M. Rudolph, D. Pare, *Nat Rev Neurosci* **4**, 739 (2003).

S9. P. C. Bush, D. A. Prince, K. D. Miller, *J Neurophysiol* **82**, 1748 (1999).

S10. M. L. Hines, T. Morse, M. Migliore, N. T. Carnevale, G. M. Shepherd, *J Comput Neurosci* **17**, 7 (2004).

S11. G. Stuart, N. Spruston, *J Neurosci* **18**, 3501 (1998).

S12. R. D. Traub, J. G. Jefferys, R. Miles, M. A. Whittington, K. Toth, *J Physiol* **481 (Pt 1)**, 79 (1994).

S13. I. Reuveni, A. Friedman, Y. Amitai, M. J. Gutnick, *J Neurosci* **13**, 4609 (1993).

S14. A. Destexhe, A. Babloyantz, T. J. Sejnowski, *Biophys J* **65**, 1538 (1993).

S15. Y. Gutfreund, Y. Yarom, I. Segev, *J Physiol* **483 (Pt 3)**, 621 (1995).

S16. A. Destexhe, D. Contreras, T. J. Sejnowski, M. Steriade, *J Neurophysiol* **72**, 803 (1994).

S17. Y. Yamada, Y. Nakazato, A. Ohga, *Br J Pharmacol* **96**, 470 (1989).

S18. E. a. K. White, A, *Cortical Circuits: Synaptic Organization of the Cerebral Cortex - Structure, Function and Theory.*, (Birkhauser, Boston, 1989).

S19. P. Poirazi, T. Brannon, B. W. Mel, *Neuron* **37**, 977 (2003).

S20. B. Ahmed, J. C. Anderson, R. J. Douglas, K. A. Martin, J. C. Nelson, *J Comp Neurol* **341**, 39 (1994).

S21. R. Srinivasan, H. J. Chiel, *Neural Comput* **5**, 200 (1993).

S22. A. Destexhe, D. Pare, *J Neurophysiol* **81**, 1531 (1999).

S23. S. J. Cruikshank, T. J. Lewis, B. W. Connors, *Nat Neurosci* **10**, 462 (2007).

S24. A. Destexhe, M. Rudolph, J. M. Fellous, T. J. Sejnowski, *Neuroscience* **107**, 13 (2001).

S25. L. E. Dobrunz, C. F. Stevens, *Neuron* **18**, 995 (1997).

S26. J. A. Varela *et al.*, *J Neurosci* **17**, 7926 (1997).

S27. M. Tsodyks, A. Uziel, H. Markram, *J Neurosci* **20**, RC50 (2000).

S28. C. Allen, C. F. Stevens, *Proc Natl Acad Sci U S A* **91**, 10380 (1994).

S29. C. F. Stevens, Y. Wang, *Neuron* **14**, 795 (1995).

S30. W. Maass, A. M. Zador, *Neural Comput* **11**, 903 (1999).

S31. K. J. Stratford, K. Tarczy-Hornoch, K. A. Martin, N. J. Bannister, J. J. Jack, *Nature* **382**, 258 (1996).

S32. Z. Gil, B. W. Connors, Y. Amitai, *Neuron* **23**, 385 (1999).

S33. R. M. Bruno, B. Sakmann, *Science* **312**, 1622 (2006).

S34. Z. F. Mainen, T. J. Sejnowski, *Science* **268**, 1503 (1995).

S35. S. Schreiber, D. Whitmer, J. M. Fellous, P. Tiesinga, T. J. Sejnowski, *Neurocomputing* **52-54**, 925 (2003).

S36. P. Reinagel, D. Godwin, S. M. Sherman, C. Koch, *J Neurophysiol* **81**, 2558 (1999).

S37. R. D. Traub, R. K. Wong, R. Miles, H. Michelson, *J Neurophysiol* **66**, 635 (1991).

S38. L. J. Borg-Graham, *MIT Thesis*, (1987).

Figure Captions

Fig. S1. The average membrane potential response increased nonlinearly with the number of synchronous inputs from **(A)** 5 synchronous synapses, **(B)** 10 synchronous synapses and **(C)** 20 synchronous synapse. The spike times on each trial were selected from the set of recorded LGN inputs from Kara et al. *(S1)*. **(A-C)** Top panels: Rastergrams of synaptic inputs. Middle panels: Superimposed somatic voltage responses. Bottom panels: Average relative membrane potential responses. Voltage traces for each synchrony magnitude were subtracted from the membrane potential trace of the zero synchrony magnitude case and averaged. **(D)** Average maximum EPSP amplitude as a function of synchrony magnitude. **(E)** The RPSM (reliability per synchrony magnitude curve).

Fig. S2. Illustration of experiments using "grouped" synapses in which 5 synapses per group each exhibit the same spike times, thus representing input from a single cell. **(A)** 5 synchronous synapses, using similar in vivo recorded spike times. **(B)** 10 synchronous synapses showing 2 groups of 5 synchronous synapses each and **(C)** 20 synchronous synapses, showing 4 groups of 5 synchronous synapses each. **(A-C)** Top panels: Rastergrams of synaptic inputs. Middle panels: Superimposed somatic voltage responses. Bottom panels: Average relative membrane potential responses. Voltage traces for each synchrony magnitude were subtracted from the membrane potential trace of the zero synchrony magnitude case and averaged. **(D)** Average maximum EPSP amplitude as a function of synchrony magnitude. **(E)** The RPSM (reliability per synchrony magnitude curve).

Fig. S3. Balance of inhibitory and excitatory background input shifts the reliability curve. The reliability, firing rate and reliability per spike (RPS) as a function of synchrony magnitude were measured while the rates of the random (Poisson) presynaptic spike trains for the 4500 excitatory (Glutamate) and 1000 inhibitory (GABA) intracortical synapses were varied. Excitatory synapses were stochastic with short term plasticity (see methods). Input was based on Kara experimental data (S*1*). **(A)** The background synaptic drive was varied while the ratio of excitatory to inhibitory input rates remained

constant at 1:5 (β=5). The slope at the inflection point increased with decreasing background drive. Reliability was high and each output spike was significant when total drive is low (Glu 0.5 spikes/sec, GABA 2.5 spikes/sec) Higher total drive significantly increased firing rate and reduced asymptotic reliability. **(B)** Varying the ratio of excitatory to inhibitory rates by changing the excitatory (Glu) input showed a similar steepening of the slope of the reliability curve around an inflection point as the Glu rate is decreased (β increased). **(C)** The slope also steepened when excitatory spike rates were fixed and the inhibitory GABA spike rates varied from 2.5 to 10 spikes/sec. At high levels of inhibition the inflection point shifted to right because significantly higher LGN synchrony was needed to overcome the hyperpolarization.

Fig. S4. Minima of Fano Factor (FF) for data and models for data shown in Fig. 2 for a range of counting window sizes. At the shortest counting window (1 msec), the minimum FF is close to unity. With larger counting windows (5 to 250 msec), the minimum FF progressively decreased. **(A)** Minimum FF from 800 trials of *in vivo* recordings *(S1)*. **(B)** Minimum FF from 800 trials of modeled data. The curve from the model approximately matched the shape from the experimental data.
(C) Fano Factor is inversely related to synchrony. The same output spike data files which varied synchrony magnitude, and were used to plot reliability and firing rate in Fig. 2, were used to calculate Fano Factor. (The counting window was set to 50 msec). Low spike count variability (low Fano Factor) occurs in the range of 20-80 synchronous synapses.

Figure S5. Gmax affects the output reliability and firing rate approximately linearly. Gmax of LGN input (across 300 synapses) was varied between 0 and 3 nS. **(A)** Reliability and **(B)** firing rate did not exhibit the nonlinear effects seen in Figure 2. These tests were conducted in the absence of input synchrony.

Table 1. Table of parameter values used for the V1 Spiny Stellate Cell (SSC), which has 3 major groupings - dendrites, axon, and soma. Parameters that applied to all groupings are listed in the general section. Other added mechanisms are shown within each group.

Table 2. Table of parameters used for the inhibitory neurons. The basket cell is based on G1.34 of V1 project from Bush et al (S*9*). All parameters with regard to the basket cell remain unchanged from the original ModelDB download (S*10*).

TABLE 1 – Parameter list for Spiny Stellate Cell (SSC)

A.

All SECTIONS		
V_init	-60 mV	Initial starting voltage
dt	0.1 msec	Simulation time step
tstop	250 msec	Simulation time duration
T	36 C	Simulation temperature
Ra	70 Ωcm	Global Axial Resistance (S*11*)
E_K	-80 mV	Potassium Reversal Potential
E_{Na}	50 mV	Sodium Reversal Potential
Inserted Mechanisms		
Leak Currents		
E_{leak}	-85 mV	Reversal potential of leak current

B.

DENDRITES		
g_{leak}	$27*10^{-5}$ S/cm2	Leak current conductance (varies according to distance from soma, see supporting materials text)
C_m	1.7 mF/cm2	Membrane capacitance, increased to account for spines (S*11*)
R_a	100 Ωcm	Axial resistance

C.

AXON		
C_m	1 mF/cm2	Membrane capacitance
g_{leak}	$1*10^{-5}$ S/cm^2	Leak conductance
R_a	10 Ωcm	Axial resistance
Inserted Mechanisms		
Hodgkin-Huxley Na/K channel		
V_{thresh}	-64 mV	Threshold voltage (S*37*)
G_{Nabar}	0.1 S/cm^2	Sodium conductance
G_{Kbar}	0.05 S/cm^2	Potassium conductance

D.

SOMA		
Cm	1.3 mF/ cm^2	Membrane capacitance
g_{leak}	$3*10^{-5}$ S/cm^2	Potassium leak channel conductance (S*11*)
R_a	1 Ωcm	Axial resistance
R_m	33,333 Ωcm^2	Specific membrane resistance (S*11*)
Hodgkin-Huxley Na/K channel		
V_{thresh}	-68 mV	Threshold voltage
g_{nabar}	0.3 S/cm^2	Sodium conductance
g_{kbar}	0.18 S/cm^2	Potassium conductance
Inserted Mechanisms		
Im current		

g_{Mbar}	0.01 S/cm2	M-current conductance
I_{AHP} channel		Slow Ca-dependent potassium current to control bursting
$[Ca]_i$	0.025 mM	Initial calcium concentration
β	0.03 $msec^{-1}$	Backward rate constant
τ_{min}	0.1 msec	Minimal value of the time constant
g_{kbar}	0.018 S/cm^2	Potassium conductance
I_{Ca} channel		
g_{bar}	0.2 S/cm^2	Calcium channel conductance
Ca decay pump		
$[Ca]_\infty$	0.005 mM	Steady state calcium ion concentration
$[Ca]_i$	0.04 mM	Initial calcium ion concentration
kd	0.02 mM	Equilibrium calcium value
kt	$1*10^{-4}$ mM/msec	Time constant of the pump
depth	1 μM	Depth of shell
taur	$1*10^{10}$ msec	Time constant of first-order decay
decay	100 msec	Decay time constant

TABLE 2- Parameter list for fast-spiking inhibitory interneuron

SOMA		
Cm	2.2125 mF/cm2	Membrane capacitance
g_{leak}	$1.475*10^{-4}$ S/cm2	Leak conductance
E_{leak}	-61 mV	Reversal potential of leak channel
Ra	200 Ωcm	Axial resistance
Hodgkin-Huxley Na/K channel		
V_{thresh}	-68 mV	Threshold voltage
g_{nabar}	0.3 S/cm^2	Sodium conductance
g_{kbar}	0.18 S/cm^2	Potassium conductance
Inserted Mechanisms		
Na channel		Sodium channel
g_{max}	0.08 S/cm^2	Maximal conductance
K channel		Potassium channel
g_{max}	0.09 S/cm^2	Maximal conductance
Ca channel		Borg-Graham channel (S*38*)
g_{max}	0.0005 S/cm^2	Maximal conductance
Calcium removal pump		
decay	100 msec	Decay time constant
Kca channel		
g_{max}	0.0025 S/cm^2	Maximal conductance
DENDRITES		
Leak current		
g_{leak}	$1.475*10^{-4}$ S/cm^2	Leak current conductance

Figure S1

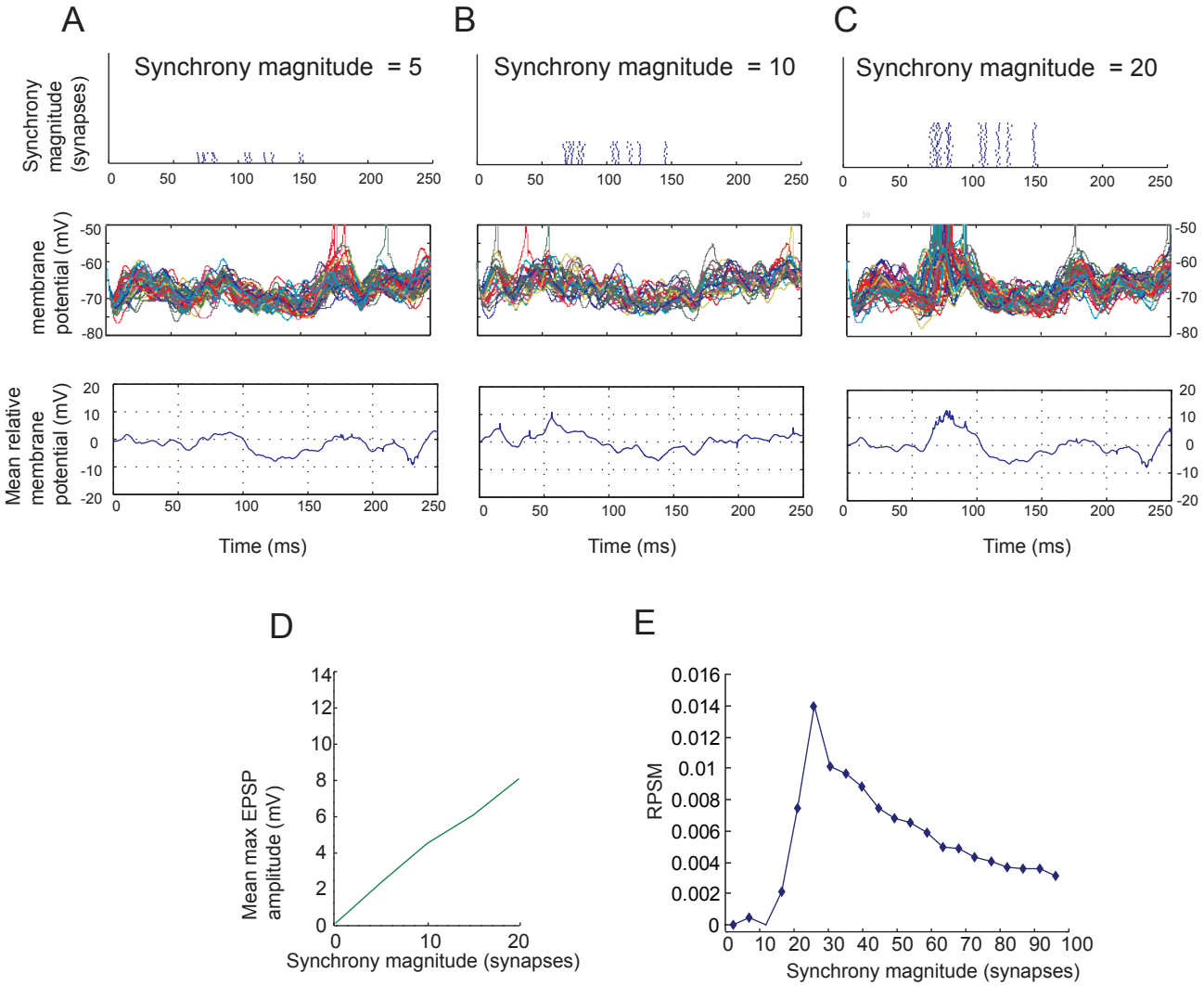
A
B
C
Synchrony magnitude = 5
Synchrony magnitude = 10
Synchrony magnitude = 20
Synchrony magnitude (synapses)
membrane potential (mV)
Mean relative membrane potential (mV)
Time (ms)
Time (ms)
Time (ms)
D
Mean max EPSP amplitude (mV)
Synchrony magnitude (synapses)
E
RPSM
Synchrony magnitude (synapses)

Figure S2

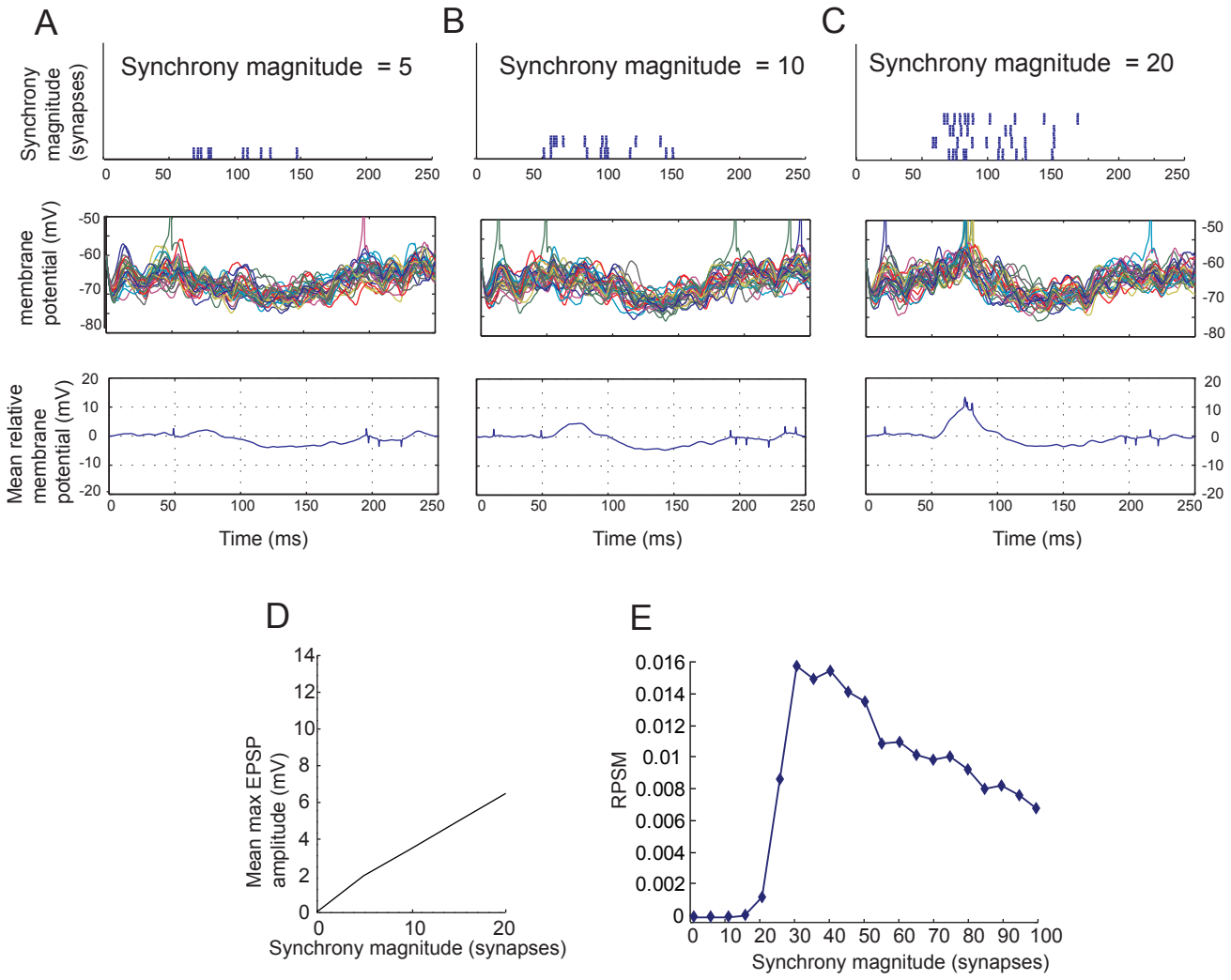
A
B
C
Synchrony magnitude = 5
Synchrony magnitude = 10
Synchrony magnitude = 20
Synchrony magnitude (synapses)
membrane potential (mV)
Mean relative membrane potential (mV)
Time (ms)
D
Mean max EPSP amplitude (mV)
Synchrony magnitude (synapses)
E
RPSM
Synchrony magnitude (synapses)

Figure S3

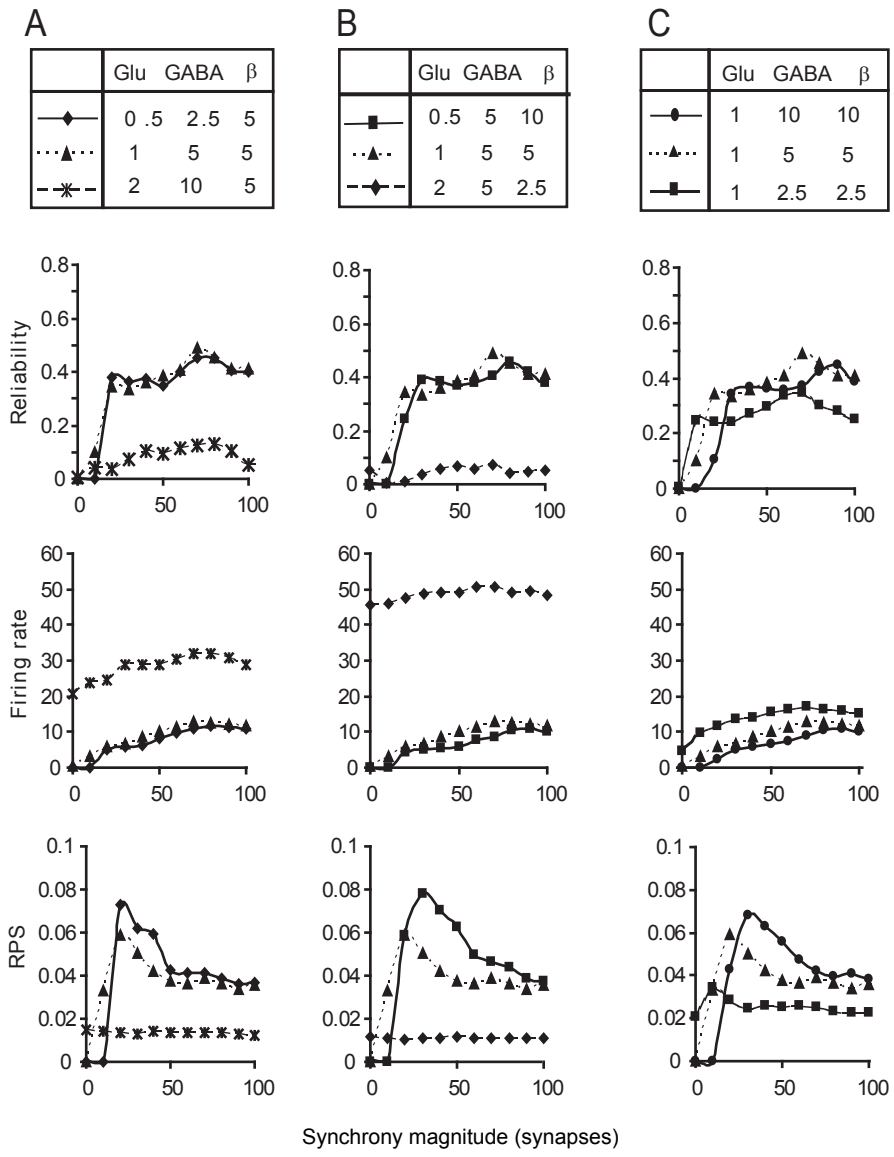
A
Glu GABA β
0.5 2.5 5
1 5 5
2 10 5
B
Glu GABA β
0.5 5 10
1 5 5
2 5 2.5
C
Glu GABA β
1 10 10
1 5 5
1 2.5 2.5
Reliability
Firing rate
RPS
Synchrony magnitude (synapses)

Figure S4

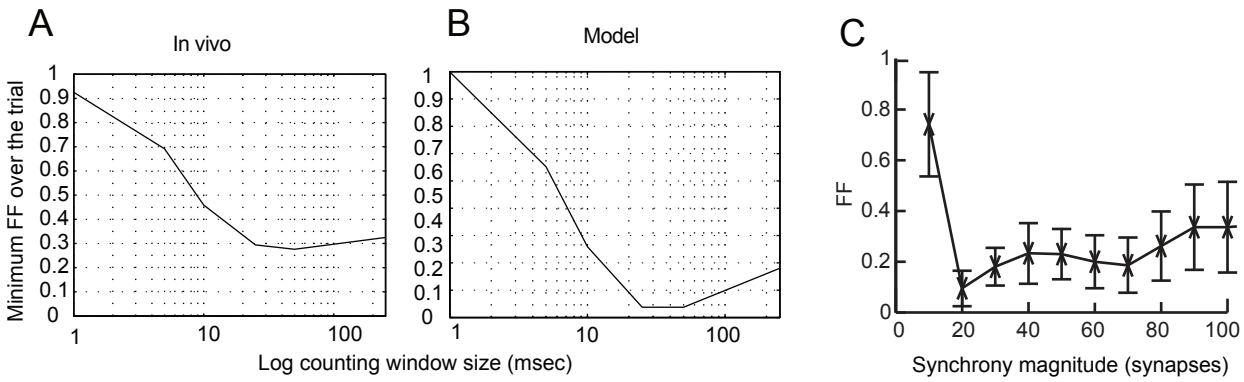
A
In vivo
B
Model
C
Minimum FF over the trial
Log counting window size (msec)
FF
Synchrony magnitude (synapses)

Figure S5

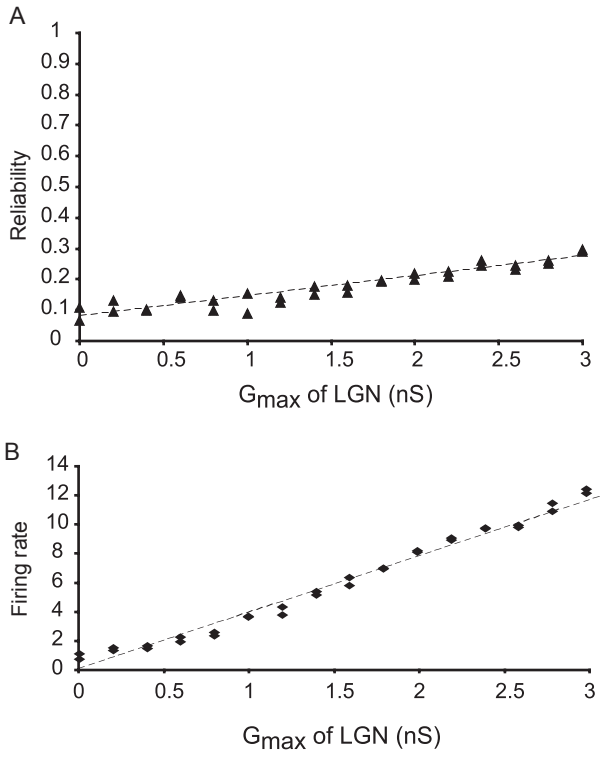
A
Reliability
1
0.9
0.8
0.7
0.6
0.5
0.4
0.3
0.2
0.1
0
0
0.5
1
1.5
2
2.5
3
Gmax of LGN (nS)
B
Firing rate
14
12
10
8
6
4
2
0
0
0.5
1
1.5
2
2.5
3
Gmax of LGN (nS)